GEOPHYSICS, VOL. 58, NO. 9 (SEPTEMBER 1993) P. 13594372, 21 FIGS, 1 TABLE.

2-D random media with ellipsoidal autocorrelation functions

L. T. Ikelle*, S. K. Yung*, and F. Daube‡

ABSTRACT

The integration of surface seismic data with borehole seismic data and well-log data requires a model of the earth which can explain all these measurements. We have chosen a model that consists of large and small scale inhomogeneities: the large scale inhomogeneities are the mean characteristics of the earth while the small scale inhomogeneities are fluctuations from these mean values.

In this paper, we consider a two-dimensional (2-D) model where the large scale inhomogeneities are represented by a homogeneous medium and small scale inhomogeneities are randomly distributed inside the homogeneous medium. The random distribution is characterized by an ellipsoidal autocorrelation function in the medium properties. The ellipsoidal autocorrelation function allows the parameterization of small scale inhomogeneities by two independent autocorrelation lengths a and b in the horizontal and the vertical Cartesian directions, respectively. Thus we can describe media in which the inhomogeneities are isotropic ($a = b$), or elongated in a direction parallel to either of the two Cartesian directions ($a > b$, $a < b$), or even taken to infinite extent in either dimension (e.g., a = infinity, b = finite: a 1-D medium) by the appropriate choice of the autocorrelation lengths.

We also examine the response of seismic waves to this form of inhomogeneity. To do this in an accurate way, we used the finite-difference technique to simulate seismic waves. Special care is taken to minimize errors due to grid dispersion and grid anisotropy. The source-receiver configuration consists of receivers distributed along a quarter of a circle centered at the source point, so that the angle between the source-receiver direction and the vertical Cartesian direction varies from 0 to 90 degrees.

Pulse broadening, coda, and anisotropy (transverse isotropy) due to small scale inhomogeneities are clearly apparent in the synthetic seismograms. These properties can be recast as functions of the aspect ratio ($r_0 = b/a$) of the medium, especially the anisotropy and coda. For media with zero aspect ratio (1-D media), the coda energy is dominant at large angles. The coda energy gradually becomes uniformly distributed with respect to angle as the aspect ratio increases to unity.

Our numerical results also suggest that, for small values of aspect ratio, the anisotropic behavior (i.e., the variations of pulse arrival times with angle) of the 2-D random media is similar to that of a 1-D random medium. The arrival times agree with the effective medium theory. As the aspect ratio increases to unity, the variations of pulse arrival times with angle gradually become isotropic. To retain the anisotropic behavior beyond the geometrical critical angle, we have used a low-frequency pulse with a nonzero dc component.

INTRODUCTION

In seismic exploration, the earth is very often approximated by a series of large homogeneous layers. Such models do not take into account small scale inhomogeneities as revealed by well logs and core samples. Furthermore, synthetic seismic data made from such models cannot explain a significant amount of variability observed in seismic field data. One alternative is a model that combines large and small scale inhomogeneities. The large scale inhomogeneities are the mean characteristics of the earth while the small scale inhomogeneities are fluctuations from these mean values. The small scale inhomogeneities are too numerous and too irregularly distributed, so the only information we

Manuscript received by the Editor June 24, 1992; revised manuscript received December 15, 1992.
*Schlumberger Cambridge Research, High Cross, Madingley Road, Cambridge CB3 OEL, England.
‡Schlumberger Laboratory for Computer Science, 8311 North RR 620, Box 200015, Austin, TX 78720-0015.
© 1993 Society of Exploration Geophysicists. All rights reserved.

can hope to reconstruct from seismic data are their statistical properties. Therefore we will represent the small scale inhomogeneities as a random process in space.

It is not the first time that a statistical representation is used to describe small scale inhomogeneities in seismological studies (Aki, 1969; O'Doherty and Anstey, 1971; Godfrey et al., 1980; Richards and Menke, 1983; Frankel and Clayton, 1984 and 1986; Lenoach, 1987; Burridge and Chang, 1988, 1989; Stanke and Burridge, 1990; Toksöz and Charette, 1990; de Hoop et al., 1991a and b; Kerner, 1992). These works have covered two types of models of small scale inhomogeneities: the finely layered medium and the two-dimensional/three-dimensional (2-D/3-D) isotropic random medium. The finely layered medium consists of a stack of a large number of plane homogeneous layers. The layers are also assumed fine, even finer than the actual sonic log resolution (de Hoop et al., 1991a). The advantage of this model is that the properties of rock formations can be described as measured by density and sonic logs, especially if it is assumed that layers are isotropic elastic. But the finely layered model is often not realistic for simulating seismic data because seismic waves see inhomogeneities away from the wellbore, over a distance corresponding to the Fresnel zone.

The 2-D random medium with an isotropic autocorrelation function has also been used to describe the small scale inhomogeneities (Frankel and Clayton, 1984). Here the inhomogeneities are isotropic and do not have any preferred orientation. It is probably realistic to consider, for the entire crust of the earth, that small scale inhomogeneities do not have a preferred orientation. In seismic exploration, we are interested in inhomogeneities in a particular rock or in a small region of the crust. For a rock or a small region of the crust, the 2-D or 3-D random medium with an isotropic autocorrelation is a restrictive model. One can imagine a rock composed of grains with systematic orientation or a region of the crust where the deposition of lenses with different lithologies has produced inhomogeneities with a preferred orientation. Our objective here is to propose a description of small scale inhomogeneities that can take into account the orientation of inhomogeneities. To achieve this objective, we will introduce a 2-D random medium with an ellipsoidal autocorrelation function. The interesting aspect of ellipsoidal autocorrelation functions is that they allow us to describe media in which the inhomogeneities are isotropic, elongated in a particular direction, or even flattened.

To take advantage of the small scale inhomogeneities in the interpretation of seismic data, we need to add a new intuition for small scale inhomogeneities to our basic intuition for large scale inhomogeneities. The new intuition will develop by the study and analysis of effects of small scale inhomogeneities on seismic data. These effects are produced from the multiple scattering of a body wave by inhomogeneities. Here, we will analyze the multiple scattering dependence with angle of incidence to the inhomogeneities for media in which the inhomogeneities are isotropic or elongated in one of the two Cartesian directions. We will use the finite-difference algorithm to simulate seismic waves. Thus multiple scattered waves, transmission losses, and surface waves are included in the waveforms.

The remainder of this paper is composed of four sections. In the first, we describe the random model with ellipsoidal autocorrelation function and show some examples. In the second section, we discuss the implementation of the finite-difference algorithm for the random model. In the third section, we examine some factors affecting multiple scattering dependence with angle, and in the fourth section, we briefly mention some implications of seismic wave propagation through small scale inhomogeneities for the interpretation of seismic data.

DESCRIPTION OF THE RANDOM MEDIUM

Setting up the problem

We start by introducing $\mathbf{m}(\mathbf{x}) = \{m_1(\mathbf{x}), m_2(\mathbf{x}), m_3(\mathbf{x})\}$ to be a finite set needed to describe an isotropic elastic medium, where x = (x, z) is the Cartesian vector. For instance m(x) can consist of P-wave velocity, V_P/V_S ratio, and density. From a structural point of view, m(x) contains large and small scale inhomogeneities. The size of large scale inhomogeneities is of the order of the dominant wavelength or larger; on the other hand small scale inhomogeneities are smaller than the dominant wavelength. Because small scale inhomogeneities are numerous and irregularly distributed, we choose to represent them by their statistical properties although they constitute a well-defined function. Our goal here is to describe small inhomogeneities by a few parameters.

We decompose the set m(x) into:

$$\mathbf{m}(\mathbf{x}) = \mathbf{m}^0 + \delta\mathbf{m}(\mathbf{x}), \tag{1}$$

where $\mathbf{m}^0$ represents the large scale inhomogeneities, that we assume homogeneous, and $\delta\mathbf{m}(\mathbf{x})$ represent small scale inhomogeneities. We will call m(x) a random medium throughout this paper.

The most likely statistical characteristics of m(x) that we can recover from seismic data are their low-order statistical moments, especially the first two moments. Therefore we will limit ourselves to second-order statistics. The first moment (i.e., the mean value) is $\mathbf{m}^0$, so $\delta\mathbf{m}(\mathbf{x})$ is a zero-mean process. The ensemble average of m(x) is:

$$\langle m_i(\mathbf{x})\rangle = m_i^0, \quad i = 1, 2, 3. \tag{2}$$

The second-order properties are specified by the two-point moment, i.e., the autocorrelation function:

$$C_i(\mathbf{x}_1, \mathbf{x}_2) = \langle m_i(\mathbf{x}_1) m_i(\mathbf{x}_2)\rangle, \quad i = 1, 2, 3. \tag{3}$$

We do not calculate the crosscorrelations between the three parameters $m_1(\mathbf{x})$, $m_2(\mathbf{x})$, and $m_3(\mathbf{x})$ because we suppose that they are independent. The correlation between the elastic parameters is still an open question; this question is beyond the scope of this text. Here, we simply choose three parameters (P-wave velocity, V_P/V_S ratio, and density) and assume that they are independent. Nevertheless, we will take the variance of V_P/V_S ratio much smaller than that of P-wave velocity to ensure that P-wave and S-wave velocities are correlated, but not perfectly.

We assume that the statistics of m(x) are spatially invariant with respect to spatial translation and that its three elements (i.e., $m_1(\mathbf{x})$, $m_2(\mathbf{x})$, and $m_3(\mathbf{x})$) share the same autocorrelation function. That is

$$C_i(\mathbf{x} + \mathbf{x}_1, \mathbf{x}_1) = \text{auto}(\mathbf{x}), \quad i = 1, 2, 3. \tag{4}$$

We will specify the form of auto(x) in the next subsection.

Ellipsoidal autocorrelation function

There are several possible choices for the autocorrelation functions: Gaussian, exponential, and the form proposed by von Karman (1948) are the common choices in seismological studies. In this paper, we will use the exponential autocorrelation function. Nevertheless, the results obtained here can be easily generalized to the Gaussian and von Karman autocorrelation functions.

We use the following form for the exponential autocorrelation function:

$$\mathrm{auto}(\mathbf{x}) = \mathrm{auto}(x, z) = \exp\left(-\sqrt{\frac{x^2}{a^2} + \frac{z^2}{b^2}}\right), \tag{5}$$

where a and b are the autocorrelation lengths, and auto (x) is considered ellipsoidal because the variables x and z have different scaling factors a and b, respectively. From a mathematical point of view, the investigation of a class of ellipsoidal autocorrelation functions can be reduced to that of isotropic autocorrelation functions $(a = b)$ by introducing $x' = x/a$ and $z' = z/b$. However, in the context of physical applications like seismic wave propagation, ellipsoidal autocorrelation functions are of interest since we can describe media in which the inhomogeneities are isotropic, or elongated in a direction parallel to either of the two Cartesian coordinates by an appropriate choice of the autocorrelation lengths. Figure 1 shows the models corresponding to six particular pairs (a, b) of autocorrelation lengths: (1, 1), (5, 5), (5, 1), (10, 1), (1, 20), and (1, ∞). These values are in meters. The elastic parameter represented here is the P-wave velocity. The mean velocity is 3000 m/s and the variance is 10 percent. Notice that some of the velocity fluctuations are more than 10 percent because the exponential autocorrelation function is unbounded.

Instead of autocorrelation lengths, it is sometimes useful to characterize the lateral shape of inhomogeneities of the random medium by the aspect ratio:

$$r_0 = \frac{b}{a}, \tag{6}$$

which is unity in the case of a random media with isotropic autocorrelation function and zero in the case of a one-dimensional (1 -D) vertically stratified random medium.

In addition to the variance and the autocorrelation lengths (or aspect ratio), the random medium is also characterized by its roughness. To explain the roughness of the random medium, it is convenient to limit ourselves to a 1-D random process. Like the spectrum of the exponential autocorrelation function (Figure 2), the spectra of most of the autocorrelation functions used in geophysical studies (e.g., von Karman and Gaussian) are flat to some corner wavenumber then asymptotically fall off at different rates. The roughness of the random medium is the rate of fall-off. Goff and Jordan (1988) give examples of 1-D media with several roughnesses.

Computational aspects

In Figure 3, we show how the random media are generated. The input is a uniform distribution of random numbers. The random medium is built using the fact that the Fourier transform of the autocorrelation function is the power spectrum of the random medium. The medium is later normalized to the desired variance.

The computations of random media, as a convolution of the square root of the autocorrelation function with uniformly distributed random numbers, are carried out in the space of continuous function. Unfortunately, the computations are performed discretely; and as a result, some errors are introduced in the process. Due to these errors, the assumptions made in equations (2) and (4), that the random medium is stationary with a constant mean value, do not hold. To illustrate the effect of these errors, let us consider a 1-D (depth dependent) random medium (Figure 4a). The random medium was computed using the algorithm shown in Figure 3. The medium has 1024 points spaced every 0.25 m with 10 percent variance. The usual way to check the stationarity of the medium is by computing the moving average [see Marple (1987) for more details on the computations of the moving average]. The moving average over a 20-point window (Figure 4b) shows significant variations of the mean value. Notice that the variations of the mean value are different for each realization. Our next task is to reduce these variations at the level where they can be negligible compared to the overall variations of the random medium.

Let us introduce a new element into the computation of the random medium, the tapering function. If $W(k_x, k_z)$ denotes the tapering function in the Fourier domain, the random medium is now derived as follows:

$$\mathrm{Rand}(k_x, k_z) = \mathrm{auto}(k_x, k_z) W(k_x, k_z) \exp[-i\theta(k_x, k_z)], \tag{7}$$

instead of

$$\mathrm{Rand}(k_x, k_z) = \mathrm{auto}(k_x, k_z) \exp[-i\theta(k_x, k_z)], \tag{8}$$

The notations are the same as that of the algorithm in Figure 3. $W(k_x, k_z)$ is designated to reduce the power at low frequencies of the autocorrelation function. Once again, we find it convenient to start with the 1-D problem, for example a depth-dependent medium. The 1-D random medium is now computed as follows:

$$\mathrm{Rand}_1(k_z) = \mathrm{auto}_1(k_z) W_1(k_z) \exp[-i\theta_1(k_z)]. \tag{9}$$

The notations are the same as that of the algorithm in Figure 3. The subscript 1 is used to indicate that the medium is 1-D. There are several possible choices for $W_1(k_z)$ (see Marple, 1987). For example, the "raised cosine":

$$W_1(k_z) = \begin{cases} 0.54 + 0.46\cos\left(\pi\left(1 - \dfrac{k_z}{k_{zmax}}\right)\right) & \text{if } |k_z| \le k_{zmax} \\ 1 & \text{otherwise,} \end{cases} \tag{10}$$

where k_{zmax} is the length of the tapering function. Let us go back to the 1-D example described in Figure 4. With the same statistical parameters and uniform distribution of random numbers we generate a new 1-D medium (Figure 5a

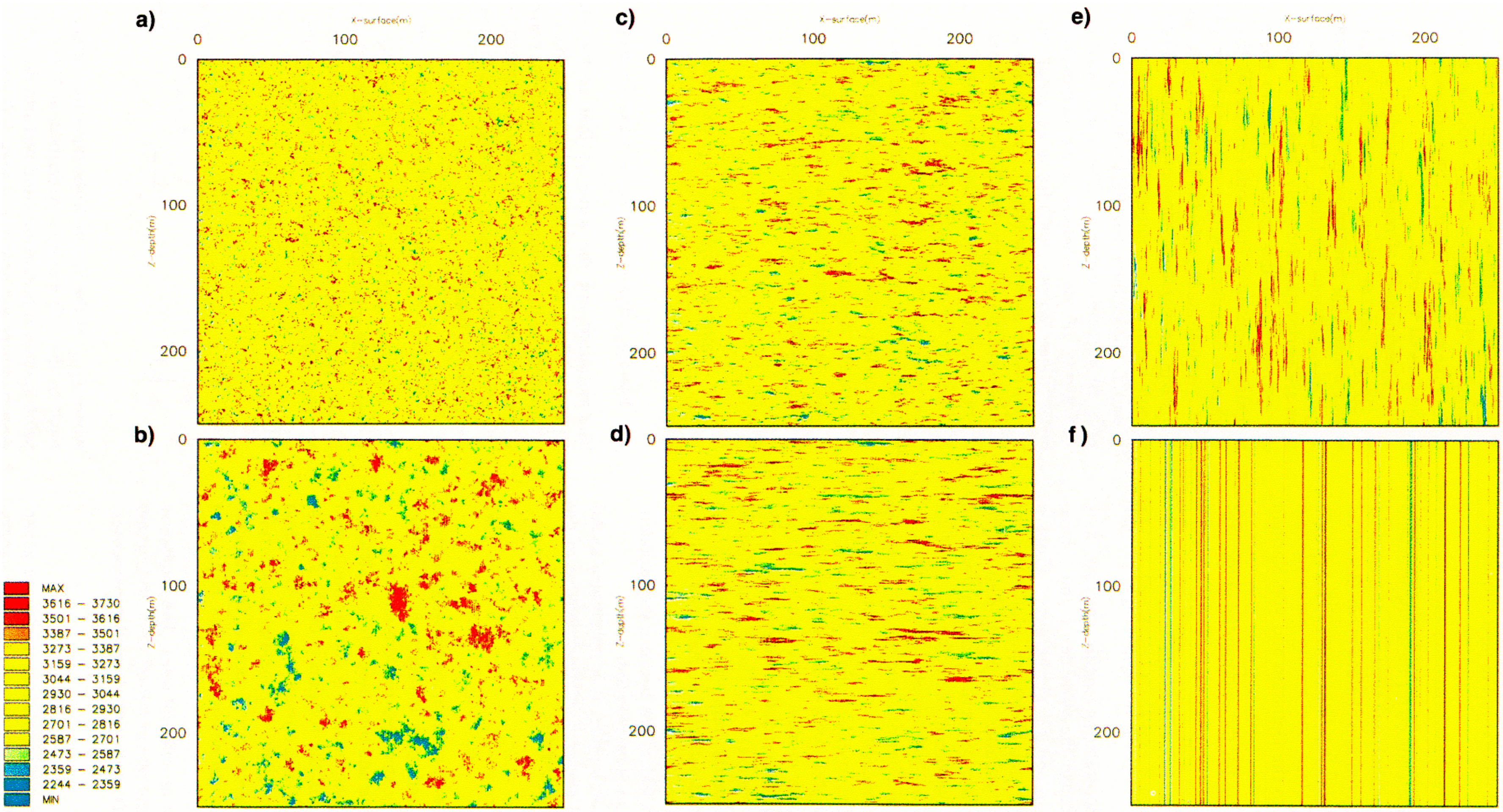

FIG. 1. Random media with an exponential autocorrelation function $f(x, z) = \exp\left[-\sqrt{(x/a)^2 + (z/b)^2}\right]$, where a and b are the autocorrelation lengths. We can describe media in which the inhomogeneities are isotropic or elongated in a direction parallel to either of the two Cartesian directions. For example, (a) represents a random media with $a = 1$ m and $b = 1$ m. (b) Same as Figure 1a with $a = 5$ m and $b = 5$ m. (c) Same as Figure 1a with $a = 5$ m and $b = 1$ m. (d) Same as Figure 1a with $a = 10$ m and $b = 1$ m. (e) Same as Figure 1a with $a = 1$ m and $b = 20$ m. (f) Same as Figure 1a with $a = 1$ m and $b = \infty$ m.

using equation (9) with the tapering function (10). The tapering length is k_{zmax} = 1.9635 m^{-1}; it corresponds to 80 points. The result of the moving average in Figure 5b, compared with Figure 4b, shows a significant reduction of the level of variations of the mean value. Now, the variations of the mean value are negligible with respect to the overall variations of the medium. These variations can be reduced further by broadening the tapering function but that might reduce the spectral resolution of the autocorrelation function. The trade-off is between the acceptable level of variation of the mean value of the random medium and the spectral resolution of the autocorrelation function. As discussed in the previous subsection, the power spectrum of the exponential autocorrelation (Figure 2) is flat to some corner wavenumber then falls off. The fall-off part of the spectrum controls the roughness of the medium. Therefore, the tapering function must stop well before the corner wavenumber of the spectrum. Because the number of points describing the flat part of the spectrum decreases when autocorrelation length increases, this trade-off implies that the tapering approach cannot be used for a large autocorrelation length.

The tapering solution can be generalized to a 2-D random medium with an ellipsoidal autocorrelation function. The tapering function must be 2-D, and it must preserve elliptical symmetries. Such a 2-D tapering function can be deduced from the 1-D tapering function via the relation

$$W(k_x,\, k_z) = W_1\left(\sqrt{k_x^2 + \frac{b^2}{a^2}\, k_z^2}\right), \tag{11}$$

where a and b are autocorrelation lengths. More details about this type of 2-D filter can be found in Huang (1972), although his analysis is limited to the case where $a = b$.

FINITE-DIFFERENCE SIMULATION IN RANDOM MEDIA

Implementation

We consider a 2-D medium with a horizontal axis x and a vertical axis z pointing downward. The medium is assumed linearly elastic and isotropic. It is also assumed to be in equilibrium at time $t = 0$, i.e., particle velocity and stress tensor are set to zero everywhere in the medium.

The elastodynamic equations can be written as a first-order hyperbolic system (Virieux, 1986):

$$\rho\,\frac{\partial v_x}{\partial t} = \frac{\partial \tau_{xx}}{\partial x} + \frac{\partial \tau_{xz}}{\partial z}, \tag{12}$$

$$\rho\,\frac{\partial v_z}{\partial t} = \frac{\partial \tau_{xz}}{\partial x} + \frac{\partial \tau_{zz}}{\partial z}, \tag{13}$$

$$\frac{\partial \tau_{xx}}{\partial t} = (\lambda + 2\mu)\,\frac{\partial v_x}{\partial x} + \lambda\,\frac{\partial v_z}{\partial z}, \tag{14}$$

$$\frac{\partial \tau_{zz}}{\partial t} = (\lambda + 2\mu)\,\frac{\partial v_z}{\partial z} + \lambda\,\frac{\partial v_x}{\partial x}, \tag{15}$$

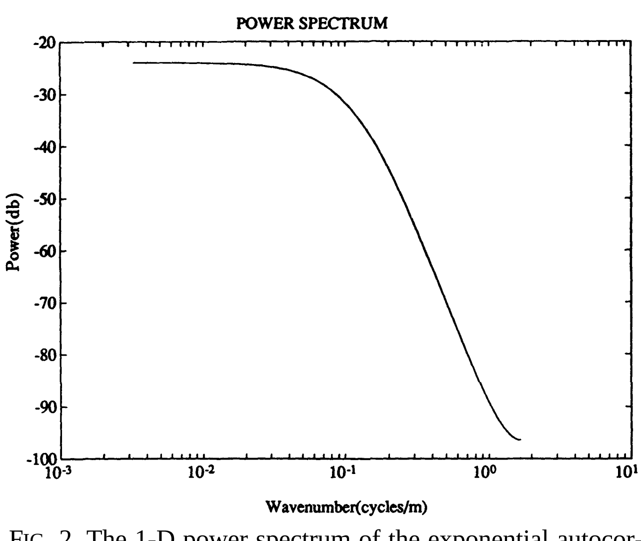

FIG. 2. The 1-D power spectrum of the exponential autocorrelation function. Notice that the spectrum is flat up to a corner wavenumber that corresponds to l/a, where a is the autocorrelation length, then asymptotically falls off.

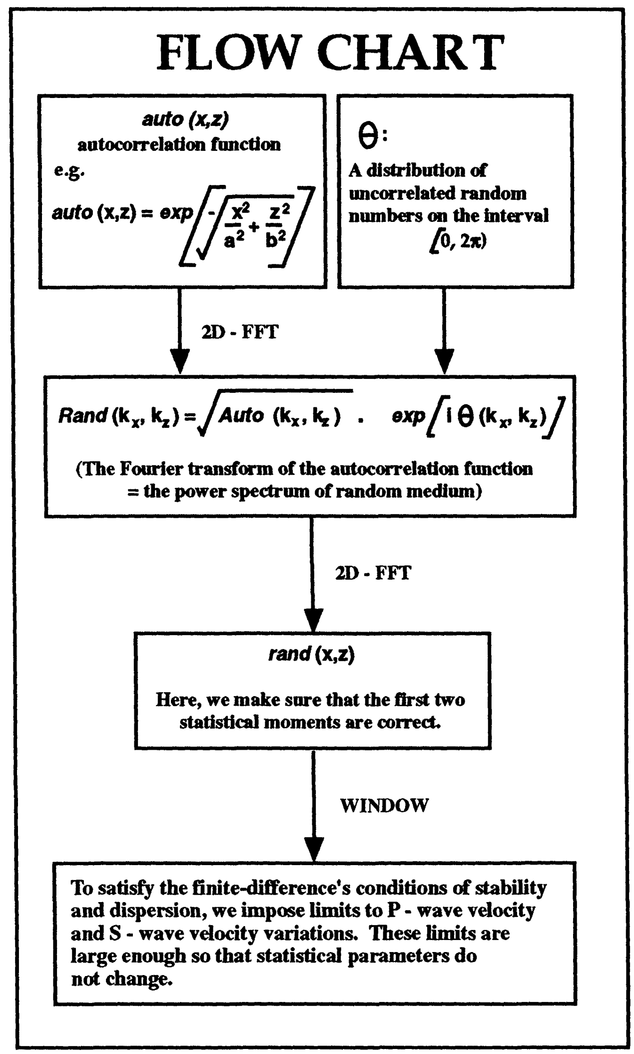

FIG. 3. Flow chart describing how the 2-D random media are generated. Two-dimensional FFT stands for two-dimensional fast-Fourier transform.

$$\frac{\partial \tau_{xz}}{\partial t} = \mu\left(\frac{\partial v_x}{\partial z} + \frac{\partial v_x}{\partial z}\right), \qquad (16)$$

where $(v_x = v_x(x, z, t), v_z = v_z(x, z, t))$ is the velocity vector, $(\tau_{xx} = \tau_{xx}(x, z, t), \tau_{zz} = \tau_{zz}(x, z, t), \tau_{zx} = \tau_{zx}(x, z, t))$ is the stress tensor, $\lambda = \lambda(x, z)$ and $\mu = \mu(x, z)$ are Lame parameters, and $\rho = \rho(x, z)$ is the density.

Equations (12) to (16) are solved numerically by the finite-difference method. The partial derivatives are replaced by their finite-difference approximations for a grid spacing of $\Delta x = \Delta z$ and a time increment Δt. We use a fourth-order approximation for spatial derivatives and a second-order approximation for the time derivative. As in Levander (1988), the velocity vector, stress tensor, Lame parameters, and density are discretized according to the Madariaga-Virieux staggered-grid formulation. The reader is referred to Madariaga (1976) and Virieux (1986) for a more detailed description of the staggered-grid formulation. We were attracted to this scheme by its high degree of accuracy and stability, especially if more than 10 gridpoints/wavelength are used. In fact, Levander's results show that grid dispersion and the grid anisotropy are insignificant if more than 10 gridpoints are used per wavelength. Furthermore, his results are valid for all values of Poisson's ratio.

In the following numerical examples, we will apply absorbing boundary conditions on all sides of the grid using the "tapering" method developed by Cerjan et al. (1985).

Accuracy tests

The accuracy test of the finite-difference scheme is the natural step that precedes the numerical experiments. It is more important here because the use of finite-difference methods for media as complex as random media might raise some anxieties. The errors in finite-difference methods can produce effects in the seismograms similar to those of attenuation, dispersion, and anisotropy. Therefore, it is necessary to ensure that these errors are not significant and that they are not contaminating our results.

We perform two accuracy tests of our finite-difference scheme by comparing seismograms from the source-receiver configuration in Figure 6 and theoretical solutions. In Figure 6, the receivers are equidistant from the source point.

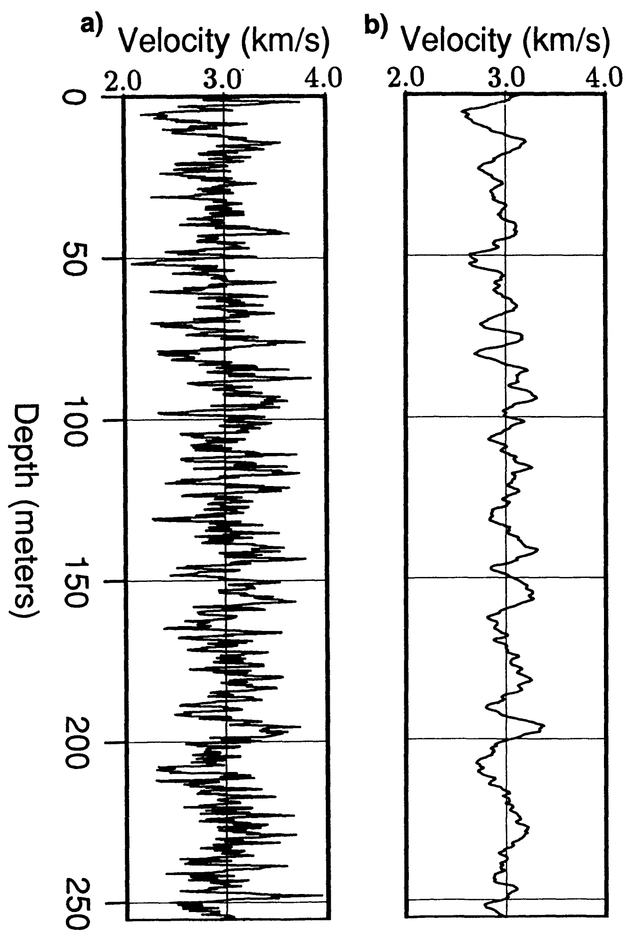

FIG. 4. (a) A 1-D random medium (P-wave velocity) generated using the algorithm described in Figure 3. (b) We take a moving average over 20 points using a boxcar window. The moving average shows significant variations of the mean velocity.

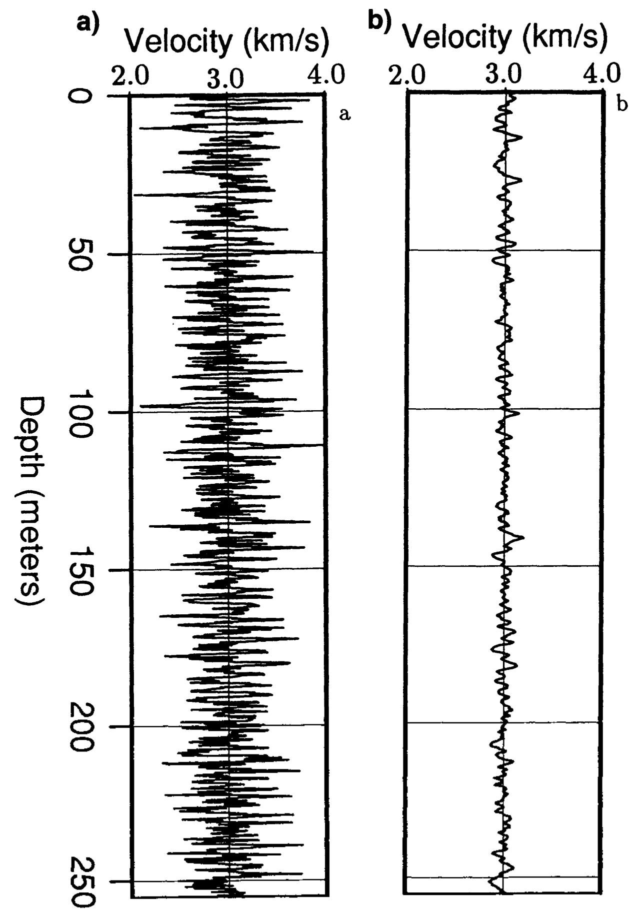

FIG. 5. (a) A 1-D random medium (P-wave velocity) generated by a modified version of the algorithm described in Figure 3 where the tapering function [equation (10)] has been included in the computation. (b) We take a moving average over 20 points using a boxcar window. Compared with Figure 4b, we see that the variations of mean velocity are negligible with respect to the overall variations of the medium.

The angle θ between the source-receiver direction and the vertical axis varies from 0 to 90 degrees. The first accuracy test is simply a verification of the radiation pattern of an explosive source in a homogeneous medium. The homogeneous medium is an infinite isotropic elastic medium where P-wave velocity is 3500 m/s, S-wave velocity is 2121 m/s and density is 2.6 g/cm^3. The wavelength for the P-wave is λ = 11.7 m and the source-receiver distance is about $L = 28\lambda$. Figures 7a and 7b show the horizontal and vertical component seismograms obtained by the finite-difference scheme. As the receivers are equidistant to the source point, the pulse arrives at the same time. The magnitude of the vertical component increases with cos θ while the magnitude of the horizontal component increases with sin θ, so that the total magnitude is invariant with θ (Figure 7c). These results agree with the radiation pattern of an explosive source (see Aki and Richards, 1980). Notice that the explosive source radiates only P-waves. Throughout this paper, we will assume an explosive source if not stated otherwise.

Our second accuracy test is performed on a 1-D random medium. We compared the traveltimes predicted by the finite-difference solution with those predicted by the effective medium theory (Backus, 1962; Schoenberg and Muir, 1989; Hsu et al., 1988). The effective medium theory gives an equivalent homogeneous transversely isotropic elastic medium to the 1-D random medium if the moving average over the 1-D random medium produces a nearly homogeneous medium. The length over which the moving average is applied must be small compared to the dominant wavelength of the signal. As discussed in the previous section, we just have to make the length of the tapering function [equation (10); k_{zmax} = 1.9635 m^{-1}] large enough to fulfill this condition. The computations of traveltime of the effective medium are described in the Appendix.

Figure 8 shows the horizontal and vertical component seismograms obtained with our finite-difference scheme. The

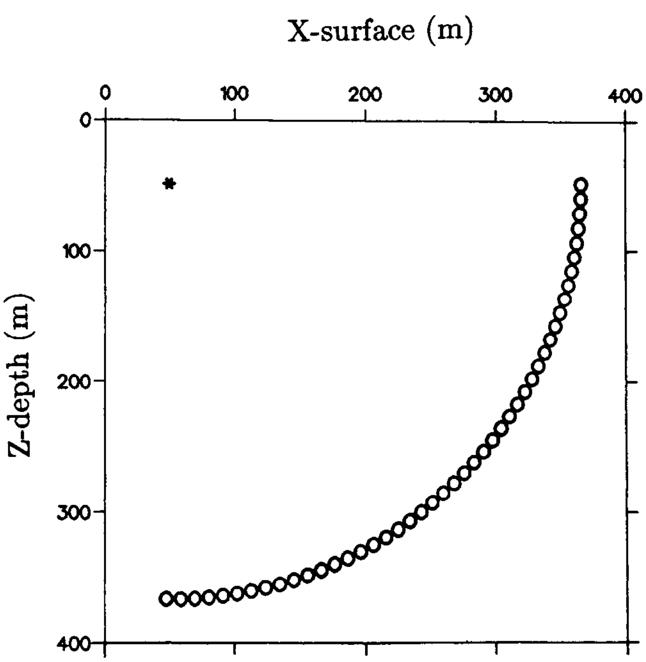

FIG. 6. The source-receiver configuration used to generate the seismograms described in this paper. The "*" represents the source position and the "o" represents the receiver positions. The receivers are distributed along a quarter of a circle so that the incident angle θ varies between 0 and 90 degrees and the receivers are equidistant from the source point.

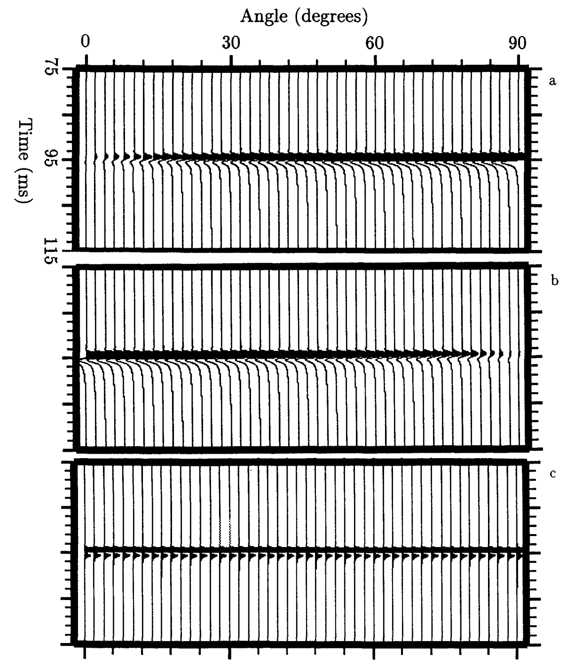

FIG. 7. Horizontal (a) and vertical (b) component seismograms corresponding to a homogeneous medium. (c) The total magnitude. The parameters of the homogeneous medium are given in Table 1. The source characteristics are also given in Table 1. Notice that the source is explosive and therefore radiates P-waves only. For the remaining figures, we will also use an explosive source except in Figure 9.

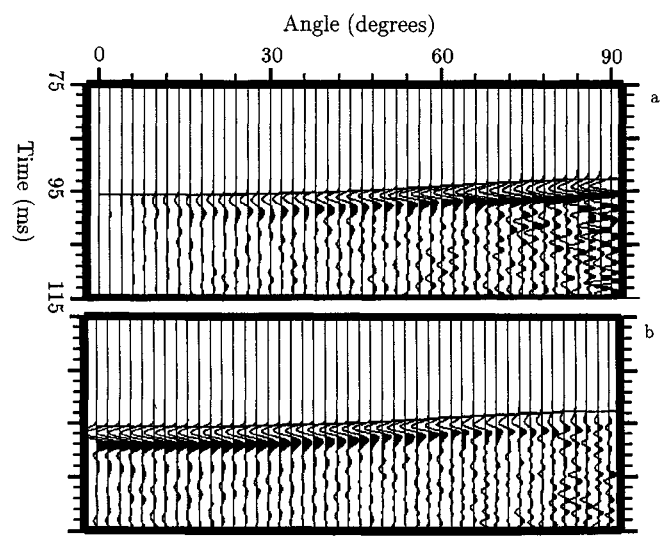

FIG. 8. Horizontal (a) and vertical (b) component seismograms corresponding to a 1-D random medium described in Table 1. The solid line represents traveltimes predicted by the effective medium theory. The fast velocity is 3509 m/s and the slow velocity is 3405 m/s.

autocorrelation length is 1.5 m (six times the grid size; Ax = Az = 0.25 m). The other elastic and statistical parameters are given in Table 1. Seismograms in Figure 8 exhibit behavior of traveltime decreasing with increasing angle of incidence. This type of behavior characterizes the anisotropy. To prove that this anisotropic behavior is due to the random medium rather than the finite-difference scheme, we have plotted the traveltimes corresponding to the effective medium in Figure 8 in a solid curve. We can notice a good agreement between the two solutions.

Another proof that the anisotropy observed in our seismograms is caused by small scale inhomogeneities is given in Figure 9. In fact, Figure 9 shows only the S-wave part of the horizontal and vertical component seismograms for the 1-D random medium used in Figure 8. This time, the seismic waves are generated by a vertical force for the vertical component and a horizontal force for the horizontal component, and the shear arrivals are recorded. If we suppose the anisotropy behavior of the P-wave is due to the finite-difference scheme, then the S-wave arrivals should have the same anisotropic pattern. Because the anistropy behavior is caused by the random medium, P-wave and S-wave arrival patterns are different and are typical of a transversely isotropic behavior. For example, the first S-wave arrival at θ = 0 degrees is at the same time as the S-wave arrival at θ = 90 degrees, while the first P-wave arrival at θ = 0 degrees is later than first P-wave arrival at θ = 90 degrees.

Up to now, we have limited the accuracy tests of the finite-difference scheme to traveltime behavior mainly because the effective medium theory is not capable of describing the other phenomena one can observe in Figures 7, 8, and 9. For example Figure 8 compared to Figure 7 shows a clear broadening of the pulse. O'Doherty and Anstey (1971), Richards and Menke (1983), Burridge and Chang (1988 and 1989) have also observed this pulse broadening effect. Furthermore, Burridge and Chang (1988 and 1989) have developed a theory that predicts this effect.

Another interesting comparison was made by Frankel and Clayton (1984). They computed synthetic seismograms from a similar fourth-order finite-difference scheme for a case of plane homogeneous acoustic layers. The velocity and density were variable at each grid point. They compare the result at normal incidence to that computed using propagator matrices (Haskell, 1960). The comparison shows an excellent agreement not only for the main pulse, but also for the coda. This result implies that the amplitudes of the synthetic seismograms are also correctly predicted by this type of finite-difference scheme. However, as observed by Frankel and Clayton (1986), Chang and Randall (1988), and Muir et al. (1992), sharp contrasts in material properties due to coarse grid spacing in a finite-difference scheme can introduce errors in modeling, especially in the coda part of the seismograms. To ensure greater accuracy in our modeling, we have chosen grid spacing to be much (at least six times) smaller than the autocorrelation lengths a and b.

SOME FACTORS AFFECTING 2-D MULTIPLE SCATTERING

Aspect ratio [equation (6)]

To see how the aspect ratio of a random medium affects the multiple scattering response, we consider six random media sharing identical statistics of the elastic parameter distributions except the aspect ratios. For each random medium, we perform a finite-difference simulation of the isotropic elastic wave equation. Figures 10-15 show vertical and horizontal component seismograms corresponding, respectively, to six aspect ratios: 0,0.05,0.1,0.2,0.5, and 1 .O. The other elastic and statistical parameters are given in Table 1.

An examination of the seismograms in Figures 10-15 allows some observations to be made about the effects of the

Table 1. Parameters used to generate synthetic data. Notice that in Figure 7 the isotropic elastic medium is homogeneous and in Figures 19 and 20 the shear velocity is constant.

Figure	f_c (Hz)	a(m)	b(m)	$r = \frac{b}{a}$	V_P (m/s)	σ_P (%)	$\frac{V_P}{V_S}$	$\sigma_{P/S}$ (%)	ρ (g/cm^3)	σ_ρ (%)	Source
7	300	N/A	N/A	N/A	3500	0	1.65	0	2.6	0	2
8	300	∞	1.5	0	3500	0	1.65	2	2.6	10	2
9	300	∞	1.5	0	3500	10	1.65	2	2.6	10	2
10	300	∞	1.5	0	3500	10	1.65	2	2.6	10	2
11	300	30	1.5	0.05	3500	10	1.65	2	2.6	10	2
12	300	15	1.5	0.1	3500	10	1.65	2	2.6	10	2
13	300	7.5	1.5	0.2	3500	10	1.65	2	2.6	10	2
14	300	3.0	1.5	0.5	3500	10	1.65	2	2.6	10	2
15	300	1.5	1.5	1.0	3500	10	1.65	2	2.6	10	2
19	350	∞	0.5	0	3500	12	1.65	12	2.6	12	1
20	350	∞	0.5	0	3500	12	1.65	12	2.6	12	2

f_c : central frequency of the source function.
a, b : autocorrelation lengths.
r : aspect ratio.
V_P, σ_P : P-wave velocity and its variance.
V_P/V_S, $\sigma_{P/S}$: ratio of P-wave velocity to S-wave velocity and its variance.
ρ, σ_ρ : density and its variance.
Source : 1 corresponds to Figure 18a and 2 corresponds to Figure 18b.

aspect ratio on the anisotropic behavior in traveltime, the coda, and the pulse broadening. Let us start with the anisotropic behavior. The decrease of pulse arrival times with the increase of incident angle, observed in Figure 10 (r_0 = 0), characterized an anisotropic behavior. As the aspect ratio increases to unity, the anisotropic behavior progressively turns to an isotropic behavior. For r_0 = 1 (Figure 15), pulse arrivals are almost invariant with the incident angles. The plots of estimated traveltime versus incident angle are depicted in Figure 16a. As the aspect ratio varies from 0 to 1, the change from anisotropic to isotropic behavior is evident. Despite the presence of strong coda, which is a correlated noise, the time picking algorithm gives a good approximation of the first pulse arrival time.

The other question concerning the anisotropic behavior is: what types of anisotropic models are related to the different aspect ratios? We know that for r_0 = 0 (i.e., 1-D medium) the pulse sees a transversely isotropic elastic medium. Figures 11-14 also show typical patterns of transversely isotropic elastic model. We can even say that, for r_0 = 0.05 (Figure 11), the pulse sees a transversely isotropic elastic medium almost identical to the one corresponding to r_0 = 0. We arrived at this conclusion by analyzing the residuals

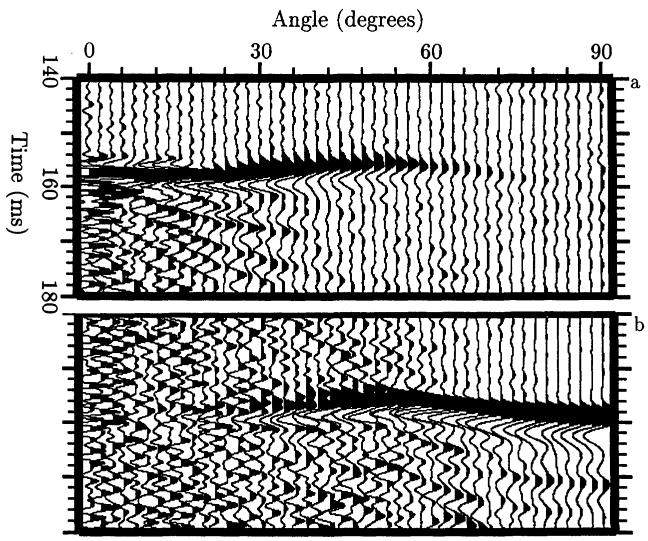

FIG. 9. S-wave part of the horizontal (a) and vertical (b) component seismograms from a 1-D random medium identical to the one used in Figure 8. Seismic waves are generated by a vertical point force for the vertical component and a horizontal point force for the horizontal component. We can see that the P-wave (Figure 8) and S-wave arrivals combined describe a transversely isotropic elastic medium. For example, the first S-wave arrival at θ = 0 degrees is at θ = 90 degrees while the first P-wave arrival at θ = P-wave arrival at θ = 90 degrees.

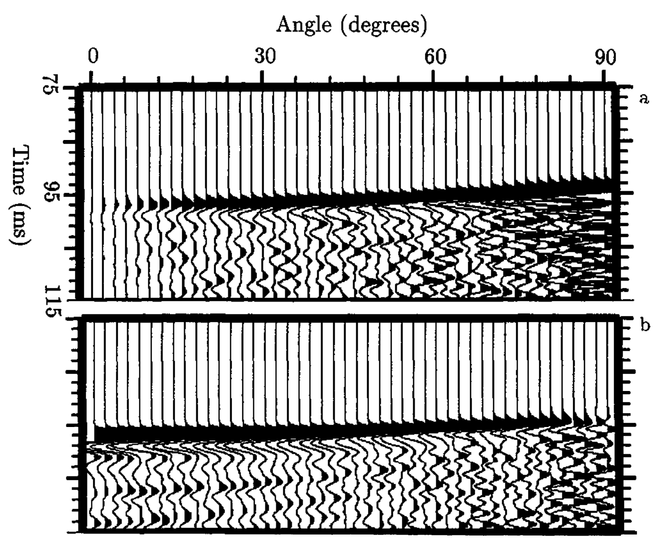

FIG. 10. Horizontal (a) and vertical (b) component seismograms corresponding to a random medium with r_0 = 0 (zero aspect ratio). The other elastic and statistical parameters are described in Table 1. The characteristics of the source function are also given in Table 1.

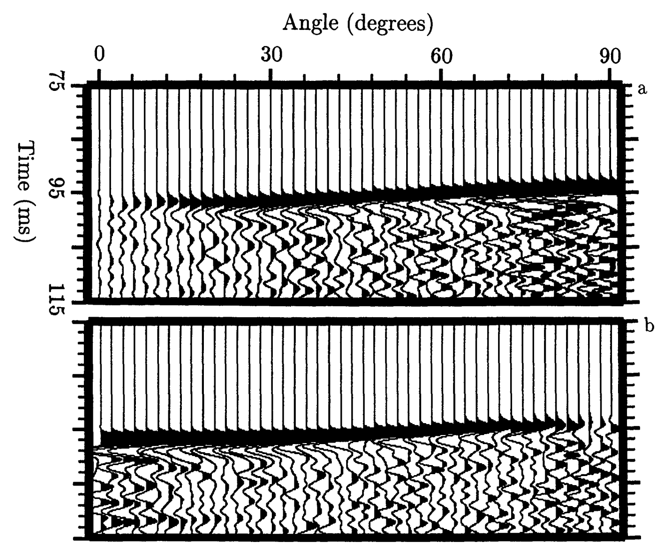

FIG. 11. Same as Figure 10 with r_0 = 0.05.

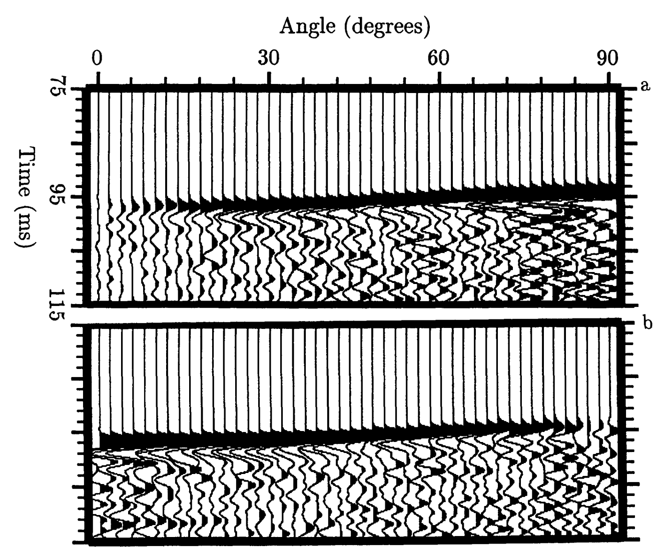

FIG. 12. Same as Figure 10 with r_0 = 0.1.

between the seismograms in Figure 10 (r_0 = 0) and those in Figure 11 (r_0 = 0.05). This conclusion indicates that, for small values of aspect ratio, the 2-D random medium can be treated anisotropically as a 1-D medium. The traveltime versus incident angle curves for r_0 = 0 and r_0 = 0.05 (Figure 16b) reiterate the similarity of anisotropic behavior. The discrepancies at large incidence angles are due to the strong coda. The problem of theoretical description of the transition from 1-D to 2-D anisotropic behavior as the aspect ratio increases requires investigations that are beyond the scope of this text.

The seismic signal in Figures 10-15 can be divided into two parts: the wavefront and the coda. The coda represents the seismic energy behind the wavefront [this definition comes from the classical papers of Aki (1969) and Aki and Chouet (1975)]. Let us make some observations on the coda energy dependence on the aspect ratio. For r_0 = 0 (Figure 10), most of the coda energy is located at large angles. As the medium is only depth dependent, this energy at large angles is essentially due to the effect of tunneling waves beyond the critical angle (early arrivals) and to guided waves that travel laterally (late arrivals). As the aspect ratio increases to one, the coda energy is essentially caused by

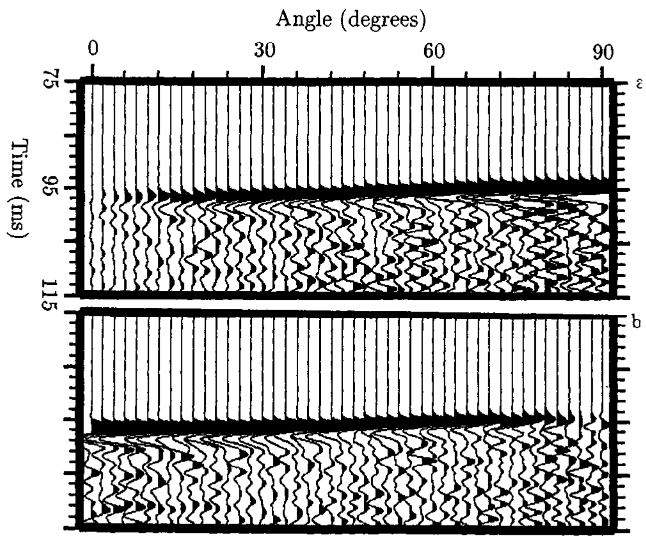

FIG. 13. Same as Figure 10 with r_0 = 0.2.

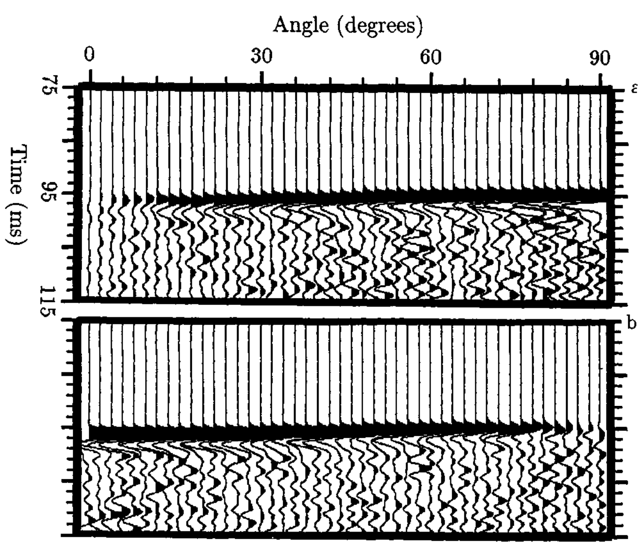

FIG. 14. Same as Figure 10 with r_0 = 0.5.

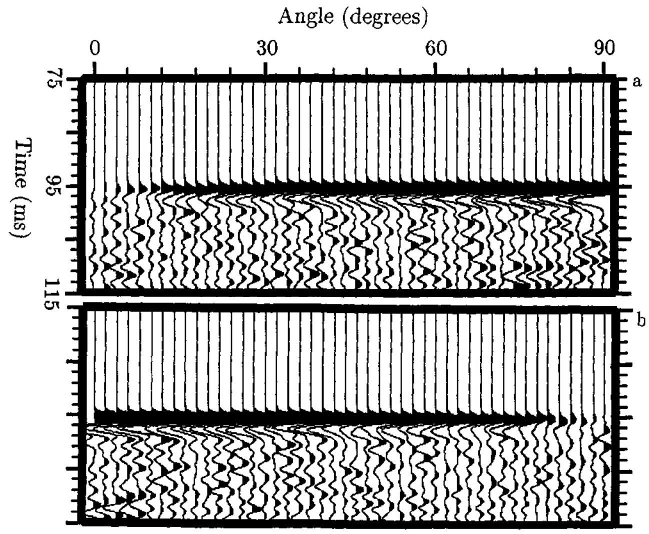

FIG. 15. Same as Figure 10 with r_0 = 1.0.

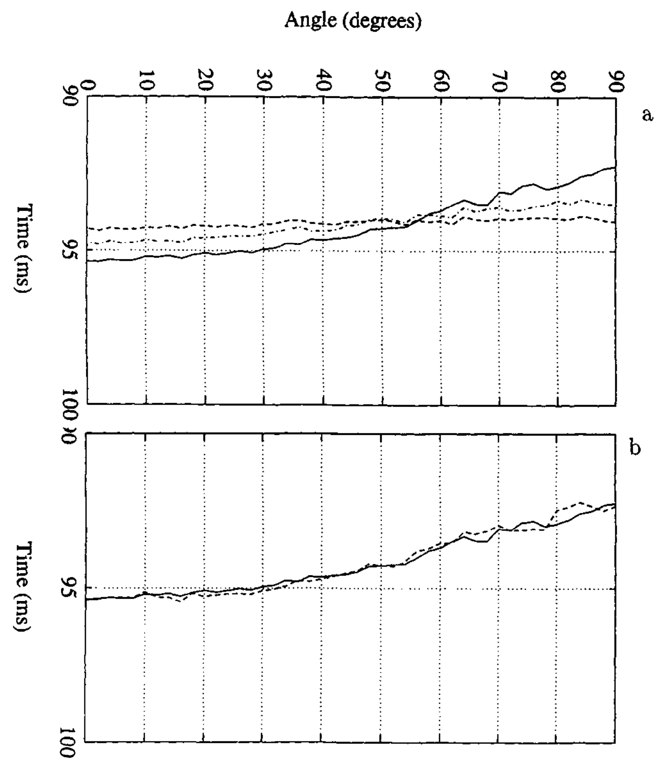

FIG. 16. Traveltime versus angles. (a) For clarity, we only show three aspect ratios: 0 (solid), 0.5 (dash-dot), and 1 (dashed). (b) Here we show two aspect ratios: 0 (solid) and 0.05 (dashed), which have a very similar traveltime/angle curve. The discrepancies at large angles are essentially due to the corruption of strong coda on the time picking algorithm.

multiple scattering of body waves. It becomes uniformly distributed with respect to angle of incidence since the model is isotropic. These results suggest that the coda might be another indicator of the aspect ratio variations.

Finally, we observe that the initial pulse in Figure 7 has been broadened in Figures 10-15 because of multiple reflection or multiple scattering. However, a closer look at the pulse in these figures shows very little changes in the pulse broadening with increasing aspect ratios (Figure 17). This observation is consistent with results from various realizations.

Seismic pulse

In the course of our numerical simulations, we have experienced how crucial the choice of the source time function is to observing features described above. For example, we have noticed that a finite-difference simulation through a 1-D random medium with a typical band-limited source cannot predict the pulse arrival above the geometric ray critical angle. Let us look at this problem in more detail. Again, we consider the source-receiver configuration in Figure 6 and a 1-D random medium. The elastic and statistical parameters of the 1-D random medium are specified in Table 1. Notice that the shear velocity is held constant. Two runs of the finite-difference modeling are made using, first, a high-frequency, band-limited pulse (Figure 18a) and second, a low-frequency, high-cut pulse (Figure 18C).

We computed both horizontal and vertical component seismograms (Figures 19 and 20) by propagating the two pulses through the 1-D model. An examination of the synthetic data allowed the following observations to be made:

1) Below the geometric ray critical angle (about 60 degree), both computations display similar behavior of traveltime decreasing with increasing angle of incidence. Because the medium is 1-D and the dominant wavelength is longer than the scale of inhomogeneities, both seismic pulses see a transversely isotropic medium;

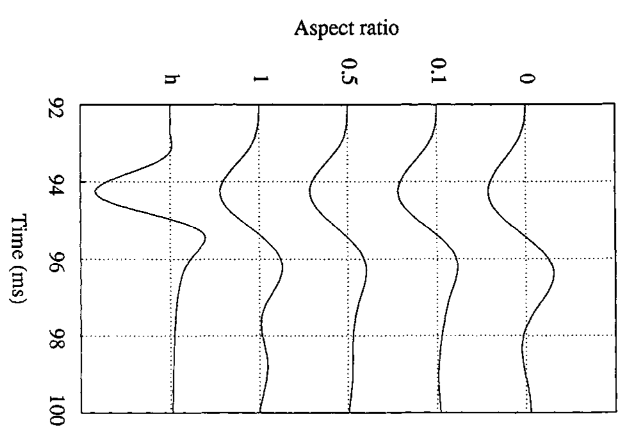

FIG. 17. Here, we show a window of vertical seismogram trace at θ = 0 degrees for the homogeneous medium (Figure 7b) and four random media (Figures 10b, 12b, 14b, and 15b), corresponding respectively to r_0 = 0, 0.1, 0.5, and 1. Notice that a correction of traveltime delays was made to enhance the comparison of pulse broadening.

2) Above the geometric ray critical angle, the first arrival curve corresponding to the high frequency pulse becomes discontinuous and the first arrival becomes incoherent. On the other hand, the low-frequency pulse retains continuity of the traveltime with a significant first arrival, albeit changed in waveshape.

We believe that the interruption in the traveltime curve of the high-frequency pulse is caused by the critical angle phenomena. Above the critical angle, strong scattering and mode conversion takes energy out of the first arrival and builds up the coda. Ray tracing through the medium (Figure 21) supports this hypothesis by indicating the presence of a weak amplitude shadow zone.

For the low-frequency pulse, which has a nonzero dc component, the layers appear thinner in wavelengths than

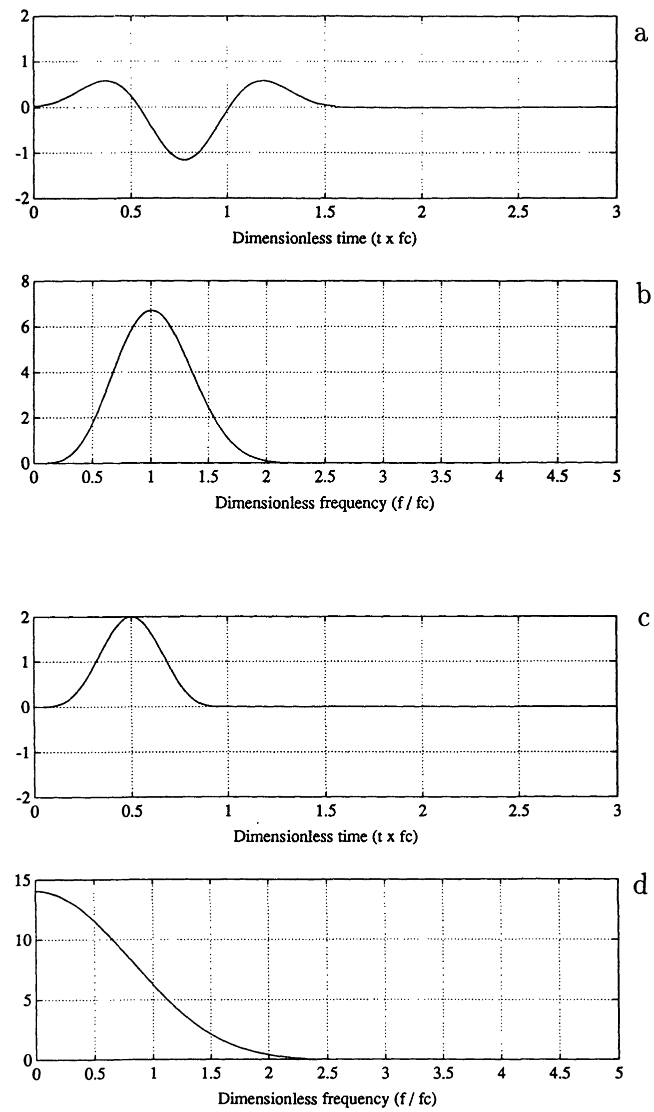

FIG. 18. (a) High-frequency, band-limited pulse and (b) its corresponding spectrum. (c) Low-frequency, high-cut pulse, and (d) its corresponding spectrum. The pulse (a) is referenced in Table 1 as type 1, and the pulse (c) is referenced in Table 1 as type 2. The parameter-f, is the central frequency.

for the high-frequency pulse. This enhances tunneling, whereby postcritical layer penetration is achieved by an evanescent leg that retains a significant amplitude in traversing the layer. This is the mechanism which we propose to fill the geometrical shadow zone and generate a first arrival.

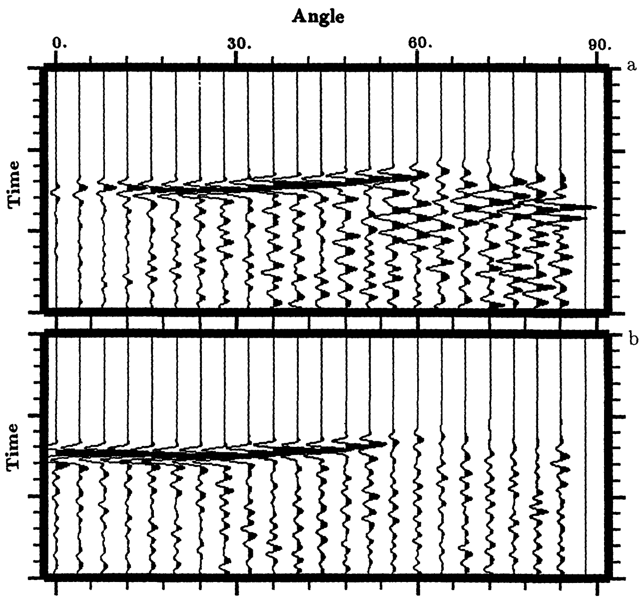

FIG. 19. Horizontal (a) and vertical (b) component seismograms corresponding to a 1-D random medium using a high-frequency, band-limited pulse (Figure 18a).

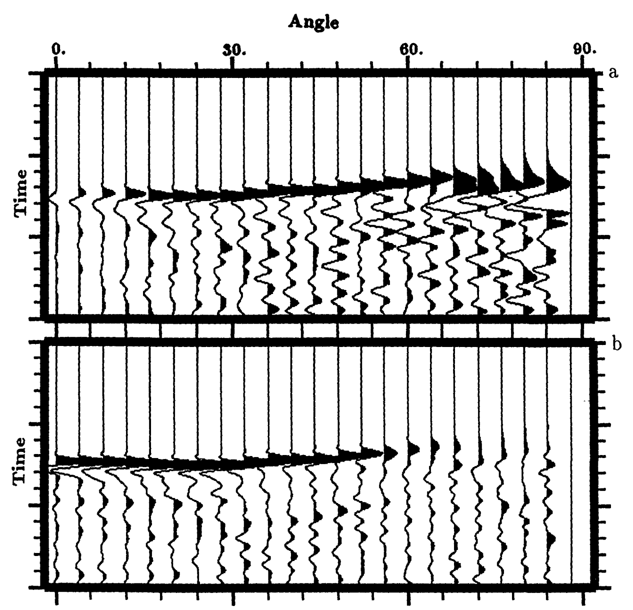

FIG. 20. Horizontal (a) and vertical (b) component seismograms corresponding to a 1-D random medium using a low-frequency, high-cut pulse (Figure 18c). Compared with Figure 19, below we see a critical angle (about 60 degree). Both figures dislay similar behavior of traveltime decreasing with angle of incidence. Above this critical angle, the first-arrival curve corresponding to high-frequency pulse (Figure 19) becomes incoherent while the low-frequency pulse retains continuity of the traveltime.

SOME IMPLICATIONS FOR SEISMIC INTERPRETATION

Seismic source function

In seismic interpretation, the lack of information about the source function is crudely compensated by a series of prestack and poststack deconvolutions. Ideally, we have to consider the source function as a parameter in the inversion or migration. If the small scale inhomogeneities are neglected as is currently the case in seismic processing, then the pulse broadening effect pointed out in this paper or in zother previous works has to be taken explicitly into account. In other words, if the earth is approximated by a series of large homogeneous layers, we would need to consider the source function not only as a time-dependent parameter but also as a space-dependent parameter.

The pulse broadening effect also explains part of the reduction of the frequency content observed in seismic field data.

Velocity model

The velocity is another critical issue in seismic interpretation, especially in the integration of surface seismic, borehole seismic, and well-log data. Here different wavelengths and different aspect ratios are involved. The modeling re-

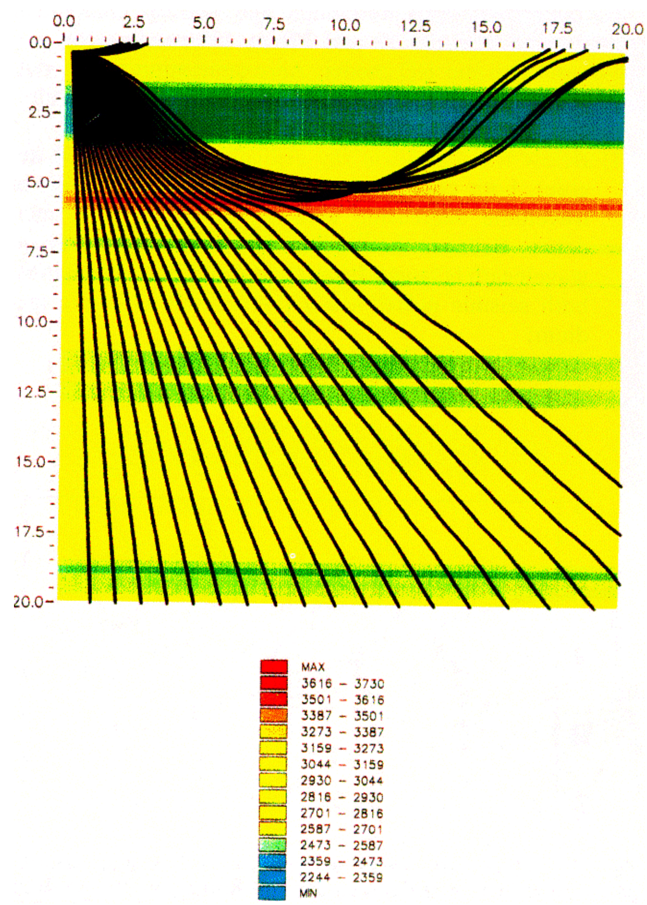

FIG. 21. Ray tracing through a 1-D medium. Only a region (20 m x 20 m) is used. Also only P -wave velocities are used.

sults shown in this paper suggest that significant discrepancies in the velocity model can occur if these parameters are neglected.

Near-surface modeling for static corrections

The near surface is one of the causes of poor resolution in land seismics. Therefore it is important to model it properly. The near surface is generally modeled as a homogeneous layer and the poor resolution is explained by the conversion of body waves into surface waves by topography at the free surface. A number of improvements have been suggested. To this list, we propose to add multiple scattering effects through the presence of small scale inhomogeneities in the homogeneous layer. A rough estimate of the aspect ratio may even be possible from the coda energy according to the modeling results reported here.

CONCLUSIONS

We demonstrated that the 2-D random medium with ellipsoidal autocorrelation function can be used to model different distributions of small scale inhomogeneities in the earth: finely layered model, isotropic random model, and model with inhomogeneities elongated in a direction parallel to either of the two Cartesian directions.

Using finite-difference modeling, we have effectively observed the pulse broadening effect, the coda, and the apparent anisotropy caused by multiple scattering in the random media. The pulse broadening effect is almost invariant with the aspect ratio, while the apparent anisotropy and coda vary with the aspect ratio. The anisotropy is a transversely isotropic behavior. This behavior increases as the incident angle increases, especially for low values of aspect ratios. It becomes isotropic (i.e., invariant with the angle of incidence) for $r_0 = 1$. The coda energy is dominant at large angles for $r_0 = 0$. It becomes uniformly distributed for $r_0 = 1$.

The observations made here suggest that small scale inhomogeneities on seismic data can be interpreted alongside large scale inhomogeneities by analyzing the pulse broadening effect, the seismic coda, and the anisotropic behavior. If such interpretation is done with constraints at space points where well-log data are available, it will lead to a model of the earth that explains both seismic and well-log data.

REFERENCES

Aki, K., 1969, Analysis of seismic coda of local earthquakes as scattered waves: J. Geophys. Res., 74, 615-631.

Aki, K., and Chouet, B., 1975, Origin of coda waves, source attenuation, and scattering effects: J. Geophys. Res., 80, 3322-3342.

Aki, K., and Richards, P. G., 1980, Quantitative seismology: Theory and methods, vols. and 2: W. H. Freeman and Co.

Backus, G., 1962, Long-wave elastic anisotropy produced by horizontal layering: J. Geophys. Res., 67, 4427-4440.

Burridge, R., and Chang, H.-W., 1988, Multimode, one-dimensional, wave propagation in a highly discontinuous medium: Wave Motion, 11, 231-249.

- 1989, Pulse evolution in a multimode, one-dimensional highly discontinuous medium, in McCarthy, M. F., and Hayes, M. A., Eds. Elastic wave propagation: Elsevier Science Publ. Co., Inc., 229-234.

Carrion, P., Costa, J., Pinheiro, J. E. F., and Schoenberg, M., 1992, Cross-borehole tomography in anisotropic media: Geophysics, 57, 1194-l 198.

Cerjan, C., Kosloff, D., Kosloff, R., and Reshef, M., 1985, A nonreflecting boundary condition for discrete acoustic-wave and elastic-wave equation: Geophysics, 50, 705-708.

Chang, H.-W., and Randall, C. J., 1988, Finite-difference time-domain modeling of elastic wave propagation in the cylindrical coordinate system: Presented at the 1988 IEEE Ultrasonic Symposium.

de Hoop, M. V., Burridge, R., and Chang, H.-W., 1991a, Wave propagation with tunneling in a highly discontinuous layered medium: Wave Motion, 13, 307-329.

——— 1991b, The pseudoprimary field due to a point-source in a finely layered medium: Geophys,. J. Int., 104, 489-506.

Frankel, A., and Clayton, R. W., 1984, A finite-difference simulation of wave propagation in two-dimensional random media: Bull., Seis. Soc. Am., 74, 2167-2186.

- 1986, Finite-difference simulations of seismic scattering: Implications for the propagation of short-period seismic waves in the crust and models of crustal heterogeneity: J. Geophys. Res., 91, 6465-6489.

Godfrey, R., Muir, F., and Rocca, F., 1980, Modeling seismic impedance with Markov chains: Geophysics, 45, 1351-1372.

Goff, J. A., and Jordan, T. H., 1988, Stochastic modeling of seafloor morphology: Inversion of sea beam data for second-order statistics: J. Geophys. Res., 93, 13 589-13 608.

Haskell, N., 1960, Crustal reflection of plane *SH-waves:* J. Geophys. Res., 65, 4147-4150.

Helbig, K., and Schoenberg, M., 1987, Anomalous polarization of elastic waves in transversely isotropic media: J. Acoust. Soc. Am., 81, 1235-1245.

Hsu, K., Esmersoy, C., and Schoenberg, M., 1988, Seismic velocities and anisotropy from high-resolution sonic logs: 58th Ann. Internat. Mtg., Soc. Expl. Geophys., Expanded Abstracts, 114-116.

Huang, T. S., 1972, Two-dimensional window: IEEE Trans. Audio electroacoustic., AU-20, 88-90.

Kerner, C., 1992, Anisotropy in sedimentary rocks modeled as random media: Geophysics, 57, 564-576.

Lenoach, B., 1987, Surface wave propagation in a random layered medium: J. Phys. A: Math. Gen., 20, 2367-2377.

Levander, A. R., 1988, Fourth-order finite-difference *P-S V* seismograms: Geophsics, 53, 1425-1436.

Madariaga, R., 1976, Dynamics of an expanding circular fault: Bull., Seis. Soc. Am., 66, 163-182.

Marple, S. L., 1987, Digital spectral analysis with applications: Prentice-Hall, Inc.

Muir, F., Dellinger, J., Etgen, J., and Nichols, D., 1992, Modeling elastic fields across irregular boundaries: Geophysics, 57, 1189-1193.

O'Doherty, R. F., and Anstey, N. A., 1971, Reflections on amplitudes: Geophys. Prosp., 19, 430-458.

Richards, P. G., and Menke, W., 1983, The apparent attenuation of a scattering medium: Bull., Seis. Soc. Am., 73, 1005-1021.

Schoenberg, M., and Muir, F., 1989, A calculus for finely layered anisotropic media: Geophysics, 54, 58 l-589.

Stanke, F. E., and Burridge, R., 1990, Comparison of spatial and ensemble averaging methods applied to wave propagation in finely layered media: 60th Ann. Internat. Mtg., Soc. Expl. Geophys., Expanded Abstracts, 1062-1065.

Toksöz, M. N., and Charette, E. E., 1990, Effects of random heterogeneities on seismic waves: Implications for determination of reservoir heterogeneities: Presented at the Soc. Expl. Geophys. Japan Int. Conf. on Geotomography.

Virieux, J., 1986, *P-SV-wave* propagation in heterogeneous media: Velocity-stress finite-difference method: Geophysics, 51, 889-901.

von Kármán, T., 1948, Progress in the statistial theory of turbulence: J. Mar. Res., 7, 252-264.

APPENDIX

A METHOD OF COMPUTATION OF TRAVELTIME FOR AN EFFECTIVE MEDIUM

Backus (1962) has developed an averaging technique to compute the elastic parameters c_{ij} for the equivalent medium from the Lame parameters (λ, μ) for a one-dimensional vertically stratified random medium. The elastic parameters are evaluated in terms of averaged algebraic expressions of the Lame parameters in the following way (Backus, 1962)

$$c_{11} = \left\langle \frac{4\mu(\lambda + \mu)}{\lambda + 2\mu} \right\rangle + \left\langle \frac{1}{\lambda + 2\mu} \right\rangle^{-1} \left\langle \frac{\lambda}{\lambda + 2\mu} \right\rangle^{2}, \tag{A-1}$$

$$c_{12} = \left\langle \frac{2\lambda\mu}{\lambda + 2\mu} \right\rangle + \left\langle \frac{1}{\lambda + 2\mu} \right\rangle^{-1} \left\langle \frac{\lambda}{\lambda + 2\mu} \right\rangle^{2}, \tag{A-2}$$

$$c_{33} = \left\langle \frac{1}{\lambda + 2\mu} \right\rangle^{-1}, \tag{A-3}$$

$$c_{13} = \left\langle \frac{1}{\lambda + 2\mu} \right\rangle^{-1} \left\langle \frac{\lambda}{\lambda + 2\mu} \right\rangle, \tag{A-4}$$

$$c_{44} = c_{55} = \left\langle \frac{1}{\mu} \right\rangle, \tag{A-5}$$

$$c_{66} = \langle \mu \rangle. \tag{A-6}$$

The angular brackets denote the moving average over a depth range ℓ'. In discrete form the moving average of a quantity f is defined as

$$\langle f \rangle_j = \sum_{k=-\ell}^{k=\ell} w_k f_{j+k}, \tag{A-7}$$

with the weighting function w_k being normalized

$$\sum_{k=-\ell}^{k=\ell} w_k = 1. \tag{A-8}$$

As Hsu et al. (1988), we choose a boxcar function $w_k = 1/(2\ell + 1)$ in a window length $\ell' = (2\ell + 1)$ as a weighting function.

For the example in Figure 8, the moving average is made over 20 points (i.e., 5 m) which produce nearly a homogeneous transversely isotropic (TI) medium. The fast compressional phase velocity is $V_P(90 \text{ degrees}) = (c_{11}/\langle p \rangle)^{1/2}$ 3509 m/s and the slow phase velocity is V_P (0 degrees) $(c_{33}/\langle \rho \rangle)^{1/2}$ = 3405 m/s.

To compute the traveltime in Figure 10, we have used group velocity that is related to c_{ij} (Helbig and Schoenberg 1984). To use Helbig and Schoenberg's formulas, let us introduce some notations:

$$C = (c_{33} + c_{11})/2, \; \gamma = c_{55}/C, \; \varepsilon_P = (c_{11} - c_{33})/2C,$$

$$e = \varepsilon_P/(1 - \gamma),$$

$$\delta = \frac{(c_{11} - c_{55})(c_{33} - c_{55}) - (c_{13} + c_{55})^2}{(c_{11} - c_{55})(c_{33} - c_{55})},$$

where C denotes the mean of c_{11} and c_{33}, γ denotes the of the square of the shear velocity along the coordinate to the mean of the squares of the compressional vel(along the coordinate axes, ε_P denotes the P-wave ε ropy factor, S denotes the anellipticity, and e is introduced only to simplify the reading of the following formula Carrion et al. (1992) for the meaningful physical se these parameters]. Then the group velocity, v_P is rel c_{ij} by

$$v_P^2[\Phi(\theta)] = f(\cos 2\theta)[1 + \sin^2 2\theta h^2(\cos 2\theta)],$$

where

$$\tan \Phi = \tan \theta \, \frac{1 - 2\cos^2 \theta h(\cos 2\theta)}{1 + \sin^2 \theta h(\cos 2\theta)},$$

$$f(x) = C[(1 - \varepsilon_P x) - (1 - \gamma)\Delta(x)],$$

$$h(x) = \frac{f'(x)}{f(x)},$$

$$\Delta(x) \simeq \frac{(1 - e^2)(1 - x^2)}{4(1 - ex)} \delta,$$

where $f'(x)$ denotes the differentiation with respect argument x, θ is the phase angle, and Φ is the gr Carrion et al. (1992) also derives a similar formula group velocity in a TI medium.